Design and Modeling of a Heat-exchange Sleeve for Enhanced Thermal Safety of Lithium-Ion Batteries

Patryck Ferreira and Shu-Xia Tang

***Abstract*— This paper presents the design and modeling of a phase change material (PCM) sleeve enclosed in a Polyethylene Terephthalate Glycol (PETG) case for the thermal management of lithium-ion batteries. The model introduces five states: PETG inner wall, PCM solid, PCM liquid, phase fraction, and PETG outer surface, ensuring accurate representation of conduction, latent heat absorption, and convective heat loss. The formulation is validated experimentally using a 26650 Li-ion cell cycled at 11 A under controlled laboratory conditions. Results show satisfactory agreement between model predictions and experimental measurements, with root-mean-square errors of $0.56\,^{\circ}\mathrm{C}$ at the PETG inner wall and $1.44\,^{\circ}\mathrm{C}$ in the PCM domain. The PETG+PCM sleeve reduces case temperature rise by approximately $5\,^{\circ}\mathrm{C}$ and attenuates oscillation amplitude, indicating the buffering role of PCM.**

***Index Terms*— Lithium-ion batteries, Phase-change material (PCM), Dynamic volume fraction, Heat-exchange sleeve, Battery safety.**

I. Introduction

Lithium-ion batteries (LiBs) are ubiquitous in applications requiring high energy density and fast charge/discharge rates, such as electric vehicles, portable electronics, and grid storage. However, as power densities increase, thermal safety becomes a critical challenge: elevated temperatures accelerate degradation, reduce performance, and in extreme cases lead to thermal runaway [1]. Passive thermal management strategies, especially those utilizing PCMs, have garnered increasing attention due to their ability to absorb latent heat and buffer temperature spikes without active cooling systems.

Beyond material selection, the structural design of PCM-based thermal management systems plays an important role in determining their effectiveness. In practical battery systems, PCMs are commonly encapsulated in shells, sleeves, or composite enclosures to ensure mechanical stability and prevent leakage during melting. The geometry, thickness, and thermal conductivity of these encapsulation structures directly influence heat-transfer pathways and the ability of the PCM to absorb and redistribute heat during high-current operation [2].

Several models for temperature in LiBs have been proposed in the literature. Early efforts focused on core/surface temperature representations [3], while more recent works introduced single- and multi-layer formulations to resolve temperature differences across internal components [4], including investigations of multilayer behavior under varied ambient conditions [5]. Building on these modeling foundations, research has also expanded toward passive thermal management using PCMs. For instance, [6] studied PCM combined with metal fins to improve temperature uniformity and mitigate hot spots, demonstrating significant reductions in peak cell temperatures. In [7], the authors reviewed LiBs cooling technologies and highlighted PCM systems as promising due to their ability to maintain more uniform temperature distributions during phase transitions, especially when integrated with other cooling strategies. Complementary studies have further explored hybrid PCM-based approaches, combining liquid cooling, air cooling with fins, or nanoparticle-enhanced PCMs to improve thermal conductivity and overall system effectiveness [8].

Despite this progress, there remain gaps in the modeling of PCM systems for battery thermal safety, especially for control-oriented or compact models that are both accurate and energy-consistent. In this work, we present a compact, energy-conserving thermodynamic model for a LiB equipped with a PCM sleeve enclosed in a PETG case. The model captures conduction through the case, separate PCM solid and liquid nodes, latent heat absorption and release via a dynamic phase-fraction, and convective loss to ambient from the outer case surface. The contributions of this paper are:

- Design and fabrication of a PETG-encapsulated PCM sleeve via CAD modeling and 3D printing, ensuring practical implementation and experimental reproducibility.
- Development of a quintuple model of a PETG-encapsulated PCM sleeve, comprising states for the PETG inner wall, PCM solid, PCM liquid, phase fraction, and PETG outer surface, ensuring representation of conduction, phase change, and convective heat loss.
- Introduction of a dynamic volume-fraction state $f(t)$, representing the instantaneous ratio of liquid to total PCM. This state explicitly captures latent-heat exchange and enables smooth solid–liquid transitions.
- Experimental validation using a 26650 LiB cycled under realistic high-current load (11 A), comparing model predictions to temperature measurements at the PETG inner wall and within the PCM, with low RMSE values ($\approx 0.56\ ^{\circ}\mathrm{C}$ and $1.44\ ^{\circ}\mathrm{C}$, respectively).
- Quantification of the thermal buffering effect of the PCM+PETG sleeve, showing a reduction in case-temperature rise of roughly $5\ ^{\circ}\mathrm{C}$ under cycling, along with attenuation of temperature oscillations.

The paper is organized as follows: Section II presents the

P. Ferreira and S.-X. Tang (corresponding author) are with the Department of Mechanical and Aerospace Engineering, Texas Tech University, Lubbock, USA. patferre@ttu.edu, shuxia.tang@ttu.edu.

design and modeling approach, Section III describes the experimental setup, Section IV reports model validation and discussion, and Section V provides the conclusion and future work.

II. Design and Modeling

This section explains the general design of the PETG+PCM sleeve and develops a compact yet physically consistent model of the PCM system enclosed in a PETG case. The aim is to capture the key thermal and phase-change dynamics using Ordinary Differential Equations (ODEs).

A. Design of the PETG+PCM sleeve

A dedicated fixture was designed to encapsulate the battery cell within a PETG sleeve filled with PCM for experimental validation of the proposed model. The sleeve geometry was chosen to provide a compact form factor with minimal added thermal resistance while maintaining structural robustness for repeated cycling. Fig. 1 illustrates the cross-sectional design: the cylindrical cell is encapsulated by a PETG shell for mechanical integrity and surrounded by a PCM. The PETG acts as both a structural enclosure and a thermal resistance, while the PCM absorbs latent heat during melting, buffering the cell temperature rise. The PETG outer surface is exposed to ambient air, enabling convective heat exchange.

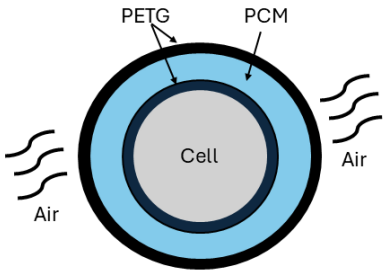

Fig. 1: Cross-sectional schematic of the PETG+PCM sleeve.

B. Modeling of the PETG+PCM structure

The fundamental heat flows between system layers are defined in Fig. 1 as a thermal resistance network (cell $\rightarrow$ PETG $\rightarrow$ PCM solid $\rightarrow$ PCM liquid $\rightarrow$ PETG $\rightarrow$ ambient), modeled using thermal resistances.

a) Cell to PETG wall.: The battery cell wall is treated as a boundary condition at temperature $T_{\text{cell}}(t)$. Heat transfer to the PETG case occurs through the thermal resistance R_{petg}:

$$Q_1(t) = \frac{T_{\text{cell}}(t) - T_{\text{petg,in}}(t)}{R_{\text{petg}}}, \tag{II.1}$$

where $T_{\text{petg,in}}(t)$ is the PETG inner wall temperature.

b) PETG wall to PCM solid lump.: The PETG transfers heat to the PCM solid domain through a thermal resistance R_{s}, representing both conduction across the PETG–PCM interface and spreading effects inside the solid PCM:

$$Q_2(t) = \frac{T_{\text{petg,in}}(t) - T_{\text{s}}(t)}{R_{\text{s}}}, \tag{II.2}$$

where $T_{\text{s}}(t)$ is the temperature of the solid PCM lump. The effective resistance R_{s} reflects geometry and material conductivity, and can be tuned against experimental data.

c) Solid PCM to liquid PCM.: Once part of the PCM has melted, solid and liquid domains coexist and exchange heat. In detailed CFD this exchange arises naturally from conduction and buoyancy-driven convection, but in lumped models it is approximated as a conductance k_{sl} multiplied by a convection boost factor $R_{\text{se}}(f(t))$ that depends on the liquid fraction:

$$Q_3(t) = R_{\text{se}}(f(t))\, k_{\text{sl}} \left(T_{\text{s}}(t) - T_{\text{l}}(t)\right), \tag{II.3}$$

where $T_{\text{l}}(t)$ is the liquid lump temperature. The dimensionless factor $R_{\text{se}}(f) \geq 1$ accounts for the enhanced heat transfer as more liquid is present. A simple choice is

$$R_{\text{se}}(f(t)) = 1 + \alpha f(t), \tag{II.4}$$

with $\alpha \geq 0$ as a tuning parameter. The factor α can be identified experimentally or estimated from effective conductivity correlations in PCM studies, and $f(t)$ denotes the liquid volume fraction of the PCM ($f = 0$ fully solid, $f = 1$ fully liquid), which evolves dynamically according to (II.12).

d) PETG Outer Case and Air Interaction: In addition to transferring heat to the PCM, the PETG enclosure also exchanges heat with the surrounding air through its outer surface. To capture this pathway, we introduce a surface node $T_{\text{surf}}(t)$ that represents the PETG outer wall temperature.

1) Inner-to-surface conduction.: Heat conduction from the PETG inner wall to the outer surface is modeled as

$$Q_4(t) = \frac{T_{\text{petg,in}}(t) - T_{\text{surf}}(t)}{R_{\text{petg,surf}}}, \tag{II.5}$$

where $R_{\text{petg,surf}}$ is the effective conduction resistance of the PETG shell.

2) Surface-to-ambient convection.: Heat loss from the PETG outer surface to the ambient air is modeled as

$$Q_5(t) = h_{\text{air}} A_{\text{air}} \big(T_{\text{surf}}(t) - T_{\text{air}}\big), \tag{II.6}$$

where h_{air} is the convective heat-transfer coefficient, A_{air} is the effective surface area exposed to air, and T_{air} is the air temperature.

C. Energy Balance

Having defined the heat flows, the energy balance at each node (PETG, PCM solid, PCM liquid) follows from the First Law of Thermodynamics. For a lumped thermal mass, the balance can be written either in total form [9]:

$$\rho c_p \dot{T}(t) = \frac{\sum Q_{\text{in}}(t) - \sum Q_{\text{out}}(t)}{V}, \tag{II.7}$$

where ρ is the density, c_p the specific heat capacity, and V the volume of the node. The term Q_{in} represents the total incoming heat flow into the node, while Q_{out} represents the total heat flow leaving the node. Applying Equation (II.7) in each node, the following expressions are obtained:

1) PETG node.: The PETG receives heat inflow $Q_1(t)$ from the battery cell and experiences two outflows: $Q_2(t)$ into the PCM solid region and $Q_4(t)$ toward the PETG surface. Its energy balance is therefore

$$\rho_{\text{petg}} c_{p,\text{petg}} \dot{T}_{\text{petg,in}}(t) = \frac{Q_1(t) - Q_2(t) - Q_4(t)}{V_{\text{petg}}}. \quad \text{(II.8)}$$

2) Solid PCM node.: The solid PCM receives heat inflow $Q_2(t)$ from the PETG and has two outflows: $Q_3(t)$ transferred to the liquid PCM domain, and the latent heat term $(1-f(t))L\dot{f}(t)$. The weighting factor $(1-f)$ ensures that the latent exchange scales with the fraction of PCM remaining in the solid phase. The corresponding energy balance is

$$\rho_{\text{s}} c_{p,\text{s}} \dot{T}_{\text{s}}(t) = \frac{Q_2(t) - Q_3(t) - (1-f(t))L\dot{f}(t)}{V_{\text{s}}}. \quad \text{(II.9)}$$

Here, we define

$$L \coloneqq m_{\text{PCM}} L_{\text{fus}}, \quad \text{(II.10)}$$

where L_{fus} is the latent heat of fusion per unit mass (J/kg), m_{PCM} is the total PCM mass.

3) Liquid PCM node.: The liquid PCM receives heat inflow $Q_3(t)$ from the solid domain and has one outflow: the latent term $f(t)L\dot{f}(t)$. This exchange is bidirectional: during melting it represents energy consumed by the liquid domain (outflow), while during solidification it returns energy to the liquid (inflow). The corresponding energy balance is given by:

$$\rho_{\text{l}} c_{p,\text{l}} \dot{T}_{\text{l}}(t) = \frac{Q_3(t) - f(t)L\dot{f}(t)}{V_{\text{l}}}. \quad \text{(II.11)}$$

Thus, when $f = 0$ no latent contribution appears in the liquid balance, and when $f = 1$ the full latent term is carried by the liquid domain.

4) Derivation of Fraction Dynamics: The volume fraction $f(t) \in [0, 1]$ represents the proportion of PCM in the liquid phase at time t. Following the relaxation principle, it is modeled as:

$$\dot{f}(t) = \frac{1}{\tau_m}\Big(f^*(T_{\text{avg}}(t)) - f(t)\Big), \quad \text{(II.12)}$$

where τ_m is the relaxation time constant. The equilibrium fraction $f^*(T_{\text{avg}}(t))$ is defined by the classical enthalpy method [10], [11]. It is piecewise linear in the mushy zone:

$$f^*(T_{\text{avg}}(t)) = \begin{cases} 0, & T_{\text{avg}}(t) \le T_{m,\text{low}}, \\ \dfrac{T_{\text{avg}}(t) - T_{m,\text{low}}}{T_{m,\text{high}} - T_{m,\text{low}}}, & T_{m,\text{low}} < T_{\text{avg}}(t) < T_{m,\text{high}}, \\ 1, & T_{\text{avg}}(t) \ge T_{m,\text{high}}, \end{cases} \quad \text{(II.13)}$$

where $T_{m,\text{low}}$ and $T_{m,\text{high}}$ denote the onset and completion temperatures of melting. The equilibrium function is evaluated at the mean PCM temperature,

$$T_{\text{avg}}(t) = \tfrac{1}{2}\big(T_{\text{s}}(t) + T_{\text{l}}(t)\big), \quad \text{(II.14)}$$

with $T_{\text{s}}(t)$ and $T_{\text{l}}(t)$ denoting the solid and liquid PCM temperatures, respectively. Equation (II.12) drives $f(t)$ toward its equilibrium value $f^*(T_{\text{avg}}(t)) \in [0, 1]$. If the initial condition satisfies $f(0) \in [0, 1]$, then $f(t)$ remains bounded in practice, although in numerical simulations it is common to enforce $f(t) \in [0, 1]$ explicitly to avoid small overshoots due to discretization.

5) Surface node.: The PETG surface temperature evolves according to the balance between conduction inflow Q_4 and convective outflow Q_5:

$$\rho_{\text{surf}} c_{p,\text{surf}} \dot{T}_{\text{surf}}(t) = \frac{Q_4(t) - Q_5(t)}{V_{\text{surf}}}. \quad \text{(II.15)}$$

This state captures the transient storage and loss of heat at the PETG–air interface, essential for accurate prediction under cycling conditions.

D. Mathematical Proof of Conservation of Energy

An essential requirement of any thermodynamic model is compliance with the First Law of Thermodynamics. Here we show that the proposed PETG+PCM system satisfies this requirement by conserving total energy.

a) Total enthalpy definition.: The total enthalpy is defined as the sum of sensible and latent contributions:

$$\begin{aligned} H(t) = {} & \rho_{\text{petg}} c_{p,\text{petg}} V_{\text{petg}} T_{\text{petg,in}}(t) + \rho_{\text{s}} c_{p,\text{s}} V_{\text{s}} T_{\text{s}}(t) \\ & + \rho_{\text{l}} c_{p,\text{l}} V_{\text{l}} T_{\text{l}}(t) + \rho_{\text{surf}} c_{p,\text{surf}} V_{\text{surf}} T_{\text{surf}}(t) + f(t)L, \end{aligned} \quad \text{(II.16)}$$

which accounts for thermal storage in the PETG inner wall, the PCM solid and liquid nodes, the PETG surface, and the latent reservoir associated with the volume fraction $f(t)$.

b) Time derivative of enthalpy.: Differentiating $H(t)$ gives

$$\begin{aligned} \dot{H}(t) = {} & \rho_{\text{petg}} c_{p,\text{petg}} V_{\text{petg}} \dot{T}_{\text{petg,in}}(t) + \rho_{\text{s}} c_{p,\text{s}} V_{\text{s}} \dot{T}_{\text{s}}(t) \\ & + \rho_{\text{l}} c_{p,\text{l}} V_{\text{l}} \dot{T}_{\text{l}}(t) + \rho_{\text{surf}} c_{p,\text{surf}} V_{\text{surf}} \dot{T}_{\text{surf}}(t) + L\dot{f}(t). \end{aligned} \quad \text{(II.17)}$$

c) Substitution of balances.: From the node balances:

$$\rho_{\text{petg}} c_{p,\text{petg}} V_{\text{petg}} \dot{T}_{\text{petg,in}}(t) = Q_1(t) - Q_2(t) - Q_4(t), \quad \text{(II.18)}$$

$$\rho_{\text{s}} c_{p,\text{s}} V_{\text{s}} \dot{T}_{\text{s}}(t) = Q_2(t) - Q_3(t) - (1-f(t))L\dot{f}(t), \quad \text{(II.19)}$$

$$\rho_{\text{l}} c_{p,\text{l}} V_{\text{l}} \dot{T}_{\text{l}}(t) = Q_3(t) - f(t)L\dot{f}(t), \quad \text{(II.20)}$$

$$\rho_{\text{surf}} c_{p,\text{surf}} V_{\text{surf}} \dot{T}_{\text{surf}}(t) = Q_4(t) - Q_5(t), \quad \text{(II.21)}$$

and substituting these into $\dot{H}(t)$ yields

$$\begin{aligned} \dot{H}(t) = {} & (Q_1(t) - Q_2(t) - Q_4(t)) + (Q_2(t) - Q_3(t) \\ & - (1-f(t))L\dot{f}(t)) + (Q_3(t) - f(t)L\dot{f}(t)) \\ & + (Q_4(t) - Q_5(t)) + L\dot{f}(t). \end{aligned} \quad \text{(II.22)}$$

d) Simplification.: The internal flows cancel exactly:

$$\begin{aligned} & -Q_2(t) + Q_2(t) = 0, \quad -Q_3(t) + Q_3(t) = 0, \\ & -Q_4(t) + Q_4(t) = 0. \end{aligned} \quad \text{(II.23)}$$

The latent terms also cancel:

$$-(1-f(t))L\dot{f}(t) - f(t)L\dot{f}(t) + L\dot{f}(t) = 0. \quad \text{(II.24)}$$

Thus the enthalpy rate reduces to

$$\dot{H}(t) = Q_1(t) - Q_5(t). \quad \text{(II.25)}$$

Remark 1. The rate of change of total enthalpy equals the external inflow $Q_1(t)$ from the cell minus the outflow $Q_5(t)$ to the ambient. All internal exchanges between PETG, PCM solid, PCM liquid, the surface, and the latent reservoir cancel identically, demonstrating that the model is internally conservative.

E. System Formulation

The extended PETG+PCM model can be expressed in compact nonlinear state–space form. The state vector is defined as

$$\mathbf{T}(t) = \begin{bmatrix} T_{\text{petg,in}}(t) & T_{\text{s}}(t) & T_{\text{l}}(t) & f(t) & T_{\text{surf}}(t) \end{bmatrix}^{tr}, \tag{II.26}$$

where the components correspond to the PETG inner-wall temperature, the solid PCM temperature, the liquid PCM temperature, the liquid fraction $f(t) \in [0, 1]$, and the PETG outer-surface temperature.

Remark 2. The phase fraction $f(t)$ is included as a system state because it evolves according to its own ODE and represents the latent-heat reservoir of the PCM. Its dynamics are driven by the average PCM temperature $T_{\text{avg}}(t)$, making $f(t)$ a state whose evolution depends on other thermal states. Including $f(t)$ in the state vector ensures both energy conservation and correct latent-heat dynamics.

The input vector collects the boundary conditions, the battery case temperature $T_{\text{cell}}(t)$ and the ambient air temperature $T_{\text{air}}(t)$:

$$\mathbf{u}(t) = \begin{bmatrix} T_{\text{cell}}(t) & T_{\text{air}}(t) \end{bmatrix}^{tr}. \tag{II.27}$$

The governing dynamics are

$$\dot{T}_{\text{petg,in}}(t) = \frac{1}{\rho_{\text{petg}} c_{p,\text{petg}} V_{\text{petg}}} \Big(\frac{T_{\text{cell}}(t) - T_{\text{petg,in}}(t)}{R_{\text{petg}}} - \frac{T_{\text{petg,in}}(t) - T_{\text{s}}(t)}{R_{\text{s}}} - \frac{T_{\text{petg,in}}(t) - T_{\text{surf}}(t)}{R_{\text{petg,surf}}} \Big), \tag{II.28}$$

$$\dot{T}_{\text{s}}(t) = \frac{1}{\rho_{\text{s}} c_{p,\text{s}} V_{\text{s}}} \Big(\frac{T_{\text{petg,in}}(t) - T_{\text{s}}(t)}{R_{\text{s}}} - R_{\text{se}}(f(t))\, k_{\text{sl}} \big(T_{\text{s}}(t) - T_{\text{l}}(t)\big) - \big(1 - f(t)\big) L \frac{1}{\tau_m} \Big(f^*(T_{\text{avg}}(t)) - f(t) \Big) \Big), \tag{II.29}$$

$$\dot{T}_{\text{l}}(t) = \frac{1}{\rho_{\text{l}} c_{p,\text{l}} V_{\text{l}}} \big(R_{\text{se}}(f(t))\, k_{\text{sl}} \big(T_{\text{s}}(t) - T_{\text{l}}(t)\big) - f(t) L \frac{1}{\tau_m} \Big(f^*(T_{\text{avg}}(t)) - f(t) \Big) \Big), \tag{II.30}$$

$$\dot{f}(t) = \frac{1}{\tau_m} \Big(f^*(T_{\text{avg}}(t)) - f(t) \Big), \tag{II.31}$$

$$\dot{T}_{\text{surf}}(t) = \frac{1}{\rho_{\text{surf}} c_{p,\text{surf}} V_{\text{surf}}} \Big(\frac{T_{\text{petg,in}}(t) - T_{\text{surf}}(t)}{R_{\text{petg,surf}}} - h_{\text{air}} A_{\text{air}} \big(T_{\text{surf}}(t) - T_{\text{air}}(t) \big) \Big). \tag{II.32}$$

Here, $R_{\text{se}}(f(t)) = 1 + \alpha f(t)$ accounts for the enhanced heat transfer as the liquid fraction increases, and $f^*(T_{\text{avg}})$ is the mushy-zone equilibrium fraction defined in (II.13).

Remark 3. Consider the simplified fraction dynamics $\dot{f}(t) = a f(t) + \frac{1}{2}(T_{\text{s}}(t) - T_{\text{l}}(t))$, where a is a relaxation coefficient with units of s^{-1}. For example, $(1-f)L\dot{f} = (1-f)L(af + \frac{1}{2}(T_{\text{s}} - T_{\text{l}}))$ and $fL\dot{f} = fL(af + \frac{1}{2}(T_{\text{s}} - T_{\text{l}}))$. These expressions introduce quadratic and bilinear products such as f^2 and $f(T_{\text{s}} - T_{\text{l}})$. Such nonlinearities prevent reduction to a linear state–space form, confirming that the PETG+PCM system is fundamentally nonlinear.

The simplified dynamics are used only to illustrate nonlinearity; all simulations employ the full formulation in (II.12)–(II.13).

In experiments the most accessible measurement is the PETG inner-wall temperature, so the model output is defined as:

$$y(t) = T_{\text{petg,in}}(t). \tag{II.33}$$

Other states such as $T_{\text{s}}(t)$, $T_{\text{l}}(t)$ or $f(t)$, are not directly measurable and would require estimation.

III. Experimental Setup

This project evaluates a PETG-encapsulated PCM sleeve for buffering Li-ion cell temperatures. The setup consists of two main components: the mechanical fixture design and fabrication, and the battery cycling experiments with temperature instrumentation.

A. Fixture Design and Fabrication

1) CAD Model: A PETG enclosure was designed in SolidWorks to house the PCM around a cylindrical cell. The wall thickness was set to ≈ 1 mm to minimize added thermal resistance while maintaining sufficient printability and stiffness.

2) 3D Printing and Assembly: The enclosure was fabricated using a FlashForge Adventurer 5M with PETG filament, selected for its high glass-transition temperature and dimensional stability. After printing, the battery cell was first inserted, and then the cavity was filled with PCM. The central hole was designed with a tolerance of $+1$ mm. If the PCM were inserted first, this tolerance could be lost, making it impossible to fit the battery. Increasing the tolerance to ease assembly would instead introduce air gaps, which could significantly affect heat transfer by reducing conduction between the cell and the PCM. To avoid this issue, the assembly sequence was fixed: insert the cell first, then add the PCM. Fig. 2 shows the printed enclosure and the assembled fixture.

3) PCM Selection: Paraffin wax was selected as the PCM due to its relatively high latent heat, chemical stability, low cost, and a melting range close to the target operating window (48–53 °C). In addition, paraffin is widely available and easy to handle, making it well suited for proof-of-concept studies and laboratory validation. The PCM was melted and poured into the PETG cavity, then allowed to solidify at room temperature.

B. Temperature Measurements

Three type-K thermocouples were used, as shown in Fig. 2:

- One thermocouple affixed to the battery surface at midline to measure the case temperature. Our previous study employed three sensors (top, middle, bottom)

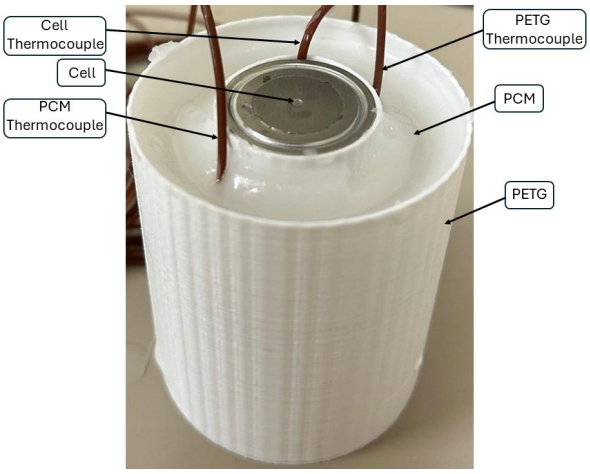

Fig. 2: 3D-printed PETG enclosure with cell, PCM and thermocouples.

along the surface and showed uniformity [4], so a single sensor is sufficient here and is used as the model input.

- One bonded to the PETG surface inside the sleeve, providing the primary validation/output signal for the model.
- One embedded in the PCM at mid-radius between the cell and the PETG wall to track the PCM temperature relative to the mushy range.

C. Battery Cycling Experiments

1) Test Bench: Cycling was performed on a NEWARE BTS-4000 system at an ambient temperature of 27 °C. The cell case temperature $T_{\text{cell}}(t)$ was measured and used as the model input.

2) Protocols: Charge/discharge profiles consisted of constant-current segments at 11 A, with a discharge cutoff of 3.45 V and a standard charge cutoff at 0.125 A.

IV. Model Validation and Discussion

Numerical simulations were performed in MATLAB R2024b using a fixed-step Runge–Kutta 4 (RK4) scheme, which provides consistent accuracy at low computational cost and ensures alignment with the experimental data. The parameters used are summarized in Table I, based on PETG material data [12] and PCM enhancements from recent studies [13].

a) Parameter calibration.: Most parameters were obtained from geometry and material data. Only k_{sl}, α, and τ_m were tuned within physically reasonable ranges to improve transient matching.

Fig. 3 shows the applied current profile during the experimental tests, consisting of repeated charge/discharge cycles at 11 A using the NEWARE BTS-4000. This profile directly drives the electrochemical reactions inside the cell, which in turn generate heat as a byproduct of internal losses.

Note that the case temperature measured under this current profile is treated as the boundary input $T_{\text{cell}}(t)$ for the PETG+PCM model. The electrochemical heat generation is therefore not modeled explicitly, but incorporated through the experimentally measured case temperature, ensuring that PCM dynamics are validated independently of detailed electrochemistry [4].

TABLE I: Model Parameters for PETG+PCM Sleeve

Parameter (Symbol)	Value	Unit
PETG Properties		
Specific heat capacity ($C_{p,\text{petg}}$)	1300	J/kgK
Density (ρ_{petg})	1270	kg/m^3
Thermal conductivity (k_{petg})	0.21	W/mK
Inner radius (r_i)	0.01325	m
Outer radius (r_o)	0.01375	m
Length (L_{petg})	0.065	m
PCM Properties		
Length (L_{pcm})	0.065	m
Solid specific heat ($C_{p,s}$)	1850	J/kgK
Liquid specific heat ($C_{p,l}$)	2384	J/kgK
Solid density (ρ_s)	930	kg/m^3
Liquid density (ρ_l)	830	kg/m^3
Solid conductivity (k_s)	7.1	W/mK
Latent heat (L_{fus})	1.9×10^5	J/kg
Inner radius ($r_{i,\text{pcm}}$)	0.01375	m
Outer radius ($r_{o,\text{pcm}}$)	0.02825	m
Solid–liquid conductance (k_{sl})	0.1	W/K
Convection boost factor (α)	1	–
Relaxation time (τ_m)	100	s

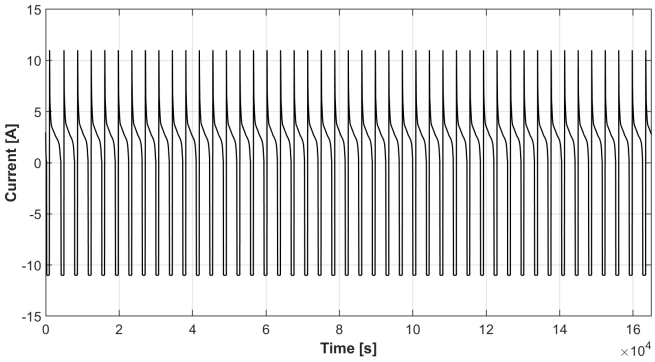

Fig. 3: Applied charge/discharge current profile (11 A) used in the NEWARE BTS-4000 experiments. The resulting case temperature serves as input to the thermal–PCM model.

Fig. 4a compares the measured PETG inner-wall temperature with the model prediction $T_{\text{petg,in}}(t)$. The agreement is excellent, with the model accurately tracking both the transient peaks during current pulses and the long-term settling value. The root-mean-square error (RMSE) is 0.56 °C, indicating that the dominant PETG dynamics are well captured. Fig. 4b validates the PCM response against the average PCM temperature, which is particularly sensitive to phase-change dynamics. The model reproduces the overall heating trend and steady-state level, but slightly overestimates the oscillation peaks. The RMSE is 1.44 °C, acceptable given the simplifications of the lumped formulation. PCM temperature discrepancies stem from: (i) unresolved spatial gradients, (ii) parameter uncertainties, and (iii) nonuniform melting fronts.

Fig. 5 shows the simulated PETG+PCM states under the experimental case-temperature input. Panel (a) depicts the experimental case-temperature input, with oscillatory peaks near 48 °C that drive the dynamics. Panel (b) presents the temperatures, where $T_{\text{petg,in}}$ and T_{s} remain closely aligned

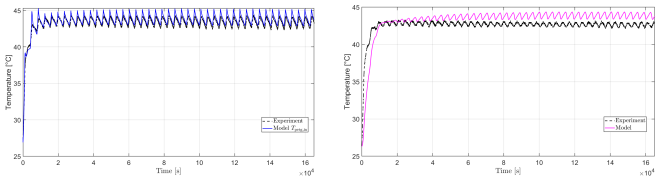

(a) PETG inner wall. (b) PCM average.

Fig. 4: Validation of the PETG+PCM model against experimental data.

due to conduction, while T_{surf} is slightly cooler due to convection and T_{l} evolves more slowly owing to latent buffering. Panel (c) shows the liquid fraction, which stabilizes around $f \approx 0.1$, indicating that only a small portion of the PCM melts. Overall, the five-state model reproduces the expected buffering behavior and demonstrates that even partial melting suffices to attenuate case-temperature oscillations.

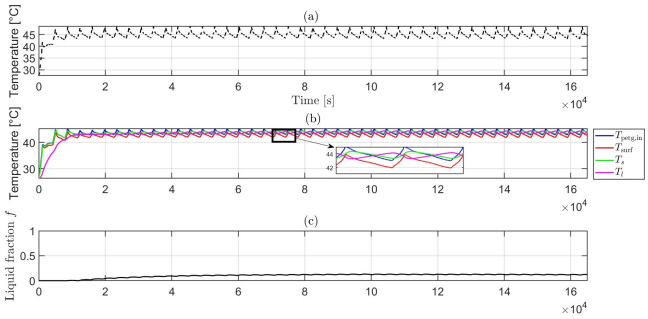

Fig. 5: Simulated PETG+PCM model states under experimental case-temperature input: (a) experimental input $T_{\text{cell}}(t)$, (b) temperatures, (c) PCM liquid fraction $f(t)$.

Fig. 6 compares the experimental case temperature of the cell with and without the PCM sleeve under the current profile of Fig. 3. The blue solid line corresponds to the bare cell, while the red dashed line represents the PETG+PCM configuration. Without PCM, the case temperature exhibits

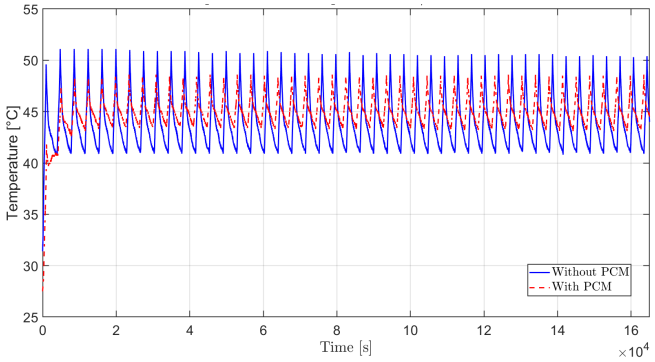

Fig. 6: Comparison of case temperature with and without PCM under 11 A cycling.

strong oscillations that follow the current pulses, peaking above 50 °C. With PCM, the maximum temperature is reduced by about 5 °C ($\sim$ 10% reduction) and capped near 45 °C. The PCM therefore absorbs and redistributes the transient heat flux, buffering the rise. These results demonstrate that the PETG+PCM sleeve not only delays heating but also reshapes the thermal dynamics by reducing both the mean and the oscillation amplitude of the case temperature. This highlights the effectiveness of phase-change buffers for LiB thermal management under high C-rate cycling.

V. Conclusion and Future Work

A compact, energy-conserving PETG+PCM model was developed and experimentally validated under high C-rate cycling. The model captures conduction, latent heat dynamics, and convection while preserving the First Law. RMSE values of 0.56 °C and 1.44 °C confirm accurate prediction of PETG and PCM temperatures. The sleeve reduced case temperature rise by approximately 5 °C and attenuated oscillations.

Due to its nonlinear state-space structure, the model is suitable for control-oriented applications such as predictive thermal monitoring and hybrid active–passive battery cooling design. Future work will extend the approach to battery packs and advanced PCMs.

References

[1] Sadiqa Jafari and Yung-Cheol Byun. Ai-driven state of power prediction in battery systems: A pso-optimized deep learning approach with xai. *Energy*, page 136764, 2025.

[2] Changcheng Liu, Dengji Xu, Jingwen Weng, Shujia Zhou, Wenjuan Li, Yongqing Wan, Shuaijun Jiang, Dechuang Zhou, Jian Wang, and Que Huang. Phase change materials application in battery thermal management system: a review. *Materials*, 13(20):4622, 2020.

[3] Xinfan Lin, Anna G Stefanopoulou, Hector E Perez, Jason B Siegel, Yonghua Li, and R Dyche Anderson. Quadruple adaptive observer of the core temperature in cylindrical li-ion batteries and their health monitoring. In *2012 American Control Conference (ACC)*, pages 578–583. IEEE, 2012.

[4] Patryck Ferreira and Shu-Xia Tang. Cascaded electrochemical-thermal modeling and temperature estimation for cylindrical li-ion batteries. *Journal of Energy Storage*, 124:116438, 2025.

[5] Patryck Ferreira and Shu-Xia Tang. Investigating thermal dynamics in cylindrical li-ion batteries across varied temperatures based on electrochemical principles. *Scientific Reports*, 15(1):30830, 2025.

[6] Pierluca Paciolla and Davide Papurello. Improved thermal management of li-ion batteries with phase-change materials and metal fins. *Batteries*, 10(6):190, 2024.

[7] Ping Fu, Lan Zhao, Xuguang Wang, Jian Sun, and Zhicheng Xin. A review of cooling technologies in lithium-ion power battery thermal management systems for new energy vehicles. *Processes*, 11(12):3450, 2023.

[8] Yvan Dutil, Daniel R Rousse, Nizar Ben Salah, Stéphane Lassue, and Laurent Zalewski. A review on phase-change materials: Mathematical modeling and simulations. *Renewable and sustainable Energy reviews*, 15(1):112–130, 2011.

[9] Theodore L Bergman, Adrienne S Lavine, Frank P Incropera, and David P DeWitt. *Introduction to heat transfer*. John Wiley & Sons, 2011.

[10] V Voller and M Cross. Accurate solutions of moving boundary problems using the enthalpy method. *International journal of heat and mass transfer*, 24(3):545–556, 1981.

[11] AD Brent, Vaughan R Voller, and KTJ Reid. Enthalpy-porosity technique for modeling convection-diffusion phase change: application to the melting of a pure metal. *Numerical Heat Transfer, Part A Applications*, 13(3):297–318, 1988.

[12] Rigid.ink Filaments. Petg data sheet. `https://devel.lulzbot.com/filament/Rigid_Ink/PETG%20DATA%20SHEET.pdf`, 2017. Accessed: 2025-09-15.

[13] Hossam A Nabwey and Maha A Tony. Enhancing the performance of paraffin's phase change material through a hybrid scheme utilizing sand core matrix. *Scientific Reports*, 14(1):20755, 2024.